



A Natural Transporter of Silicon and Carbon: Conversion of Rice Husks to Silicon Carbide or Carbon-Silicon Hybrid for Lithium-Ion Battery Anodes via a Molten Salt Electrolysis Approach

Zhuqing Zhao,^[a] Hongwei Xie,^[a] Jiakang Qu,^[a] Haijia Zhao,^[a] Qiang Ma,^[a] Pengfei Xing,^[a] Qiushi Song,^[a] Dihua Wang,^[b] and Huayi Yin^{*[a, c]}

The use of environment-benign and earth-abundant silicon (Si) and carbon (C) is the quest to meet the ever-increasing Li-ion battery (LIB) market. Unlike the traditional way of either extracting C or Si, here, we report a molten salt electrolysis approach to controllably extract both C and Si (e.g., C–SiC or C–Si composites) from rice husks (RHs). The RHs are the natural transporter that captures carbon dioxide (CO_2) from the air and silicic acid (H_4SiO_4) from the soil, thus supplying abundant, sustainable, and hierarchically porous C– SiO_2 composite feedstocks. In molten CaCl_2 , carbonized RHs (C–RHs) can be electrochemically reduced to the C–SiC composite that delivers a

gravimetric capacity of over 1000 mAh g^{-1} at 1000 mA g^{-1} after 400 cycles. In molten $\text{NaCl}-\text{KCl}-\text{MgCl}_2$, the C–RHs can be electrochemically reduced to C–Si composite that delivers a gravimetric capacity of 926 mAh g^{-1} at 500 mA g^{-1} after 100 cycles. The electrolytic products can be altered by the component of molten salt as well as by adjusting the applied cell voltage. Overall, we employ the photosynthesis of plants to harvest Si and C from nature and, subsequently, the molten salt electrolysis approach to preparing C–SiC and C–Si composites for low-cost and sustainable LIB anodes.

1. Introduction

Silicon (Si) and carbon (C) are the second and fifteenth most abundant elements in the earth's crust, which are indispensable for preparing functional materials that are widely used for electronics, photovoltaics, energy storage devices, etc.^[1] For example, Si is a promising high-capacity LIB anode (ca. 3579 mAh g^{-1} for $\text{Li}_{15}\text{Si}_4$),^[2] and the C–Si hybrid anode is intensively researched because C helps to alleviate the capacity fade caused by the immense volume expansion (>300%) of Si.^[3] With the ever-increasing LIB market, low-cost, environment-benign, and high-capacity anode materials are highly demanded for sustaining the electrification of transportation and renewable energy storage.^[4] Owing to its high affinity with oxygen, most Si feedstocks are in the form of oxides and

silicates in nature. Currently, the energy-intensive and high-temperature carbothermic reduction route produces liquid Si.^[5] However, the solidified Si ingot cannot be directly employed as the anode for LIBs because the particle size of battery materials should be in the range from micrometer to nanometer.^[6] Moreover, the preparation of nanoscale Si from the silane and Si halides requires elaborate procedures, resulting in the relatively high cost of nano-Si.^[7] Therefore, a straightforward and efficient approach to extracting nano- and/or micro-structured Si from silica is of pivotal importance to underpin the booming development of LIBs.

Solid-state metallothermic reduction routes use reactive metals (e.g., Mg, Al, etc.) to reduce porous or micro-/nano-silica precursors to Si powders.^[8] However, most natural silica and silicates are contained in rocks, which are not suitable for preparing nano- or micro-Si particles through a solid-state metallothermic reduction route. On the other hand, phytolith-containing plants are considered as vast and sustainable C and Si resources, and the extraction of Si- and C-based energy storage materials from the SiO_2 -containing plants is garnering immense attention.^[9] The biogenic Si and C possess significant advantages such as the porous structures, carbon-neutrality, sustainability, and wide availability.^[10] Among various phytolith-containing plants, rice is one of the most important agricultural crops supplying a large quantity of food with an annual production amount of ~420 million metric tons.^[11] Along with the production of rice, rice husks (RHs) mainly consist of lignin, cellulose, hemicellulose and hydrated silica. The hydrated silica accounts for ~15–20 wt.% of the entire rice kernel.^[12] Thus, RHs have been considered as a promising feedstock for the

[a] Z. Zhao, Dr. H. Xie, J. Qu, H. Zhao, Q. Ma, Prof. P. Xing, Dr. Q. Song, Prof. H. Yin
Key Laboratory for Ecological Metallurgy of Multimetalliferous Mineral of Ministry of Education
School of Metallurgy, Northeastern University
Shenyang, P.R. China, 110819

[b] Prof. D. Wang
School of Resource and Environmental Science
Wuhan University
Wuhan, P.R. China, 430072

[c] Prof. H. Yin
Key Laboratory of Data Analytics and Optimization for Smart Industry
Northeastern University
Shenyang, 110819, P.R. China
E-mail: yinhy@smm.neu.edu.cn

 Supporting information for this article is available on the WWW under <https://doi.org/10.1002/batt.201900091>

preparation of porous C, molecular sieves, catalysts, Si, etc.^[13] However, the current approaches valorizing RHs are producing either Si/silica or carbonaceous materials/hydrocarbons. Therefore, co-harvesting Si and C from RHs is the key to comprehensively utilizing the RHs that inhale CO₂ from the air and silicic acid from the soil (Figure S1).

The electrochemical reduction of oxides/sulfides in molten salts offers an efficient way to convert oxides/sulfides to metals and alloys,^[14] and Si has been successfully prepared by the electrochemical reduction of SiO₂ in CaCl₂-based molten salts.^[15] Instead of using commercial SiO₂, the use of RHs-derived SiO₂ takes advantage of the natural porous structure of SiO₂, which is helpful to rationally tune the structures and morphologies of the electrolytic Si. Moreover, the carbon in C-RHs can be utilized as a conductive network not only reducing the *I/R* drop during the molten salt electrolysis but also improving the Li storage performances of the electrolytic C-SiC and C-Si composites. Unlike the magnesiothermic reduction,^[8] the electrochemical reduction can be manipulated by altering electrochemical variables such as potentials, electrolytes, and the construction of the electrode. In CaCl₂-based molten salts, SiC has been prepared by the electrochemical reduction of the mixture of C and SiO₂.^[14d,16] Recently, SiC has been proven to be a good anode candidate with a high specific capacity of over 1000 mA h g⁻¹.^[17] Thus, RHs could be an excellent precursor for the preparation of SiC that inherits their nano-/micro- hierarchical structures. In addition to SiC, it is of great interest to prepare the C-Si composite which is a promising anode for LIBs. The major challenges of both the magnesiothermic and electrochemical reduction of C-RHs are to prevent the generation of thermodynamically favored SiC.

In this paper, both C-SiC and C-Si composites were synthesized from the electrolysis of C-RHs in molten salts. The as-prepared C-SiC and C-Si composites were employed as the LIB anodes, respectively. The structures, constituents, and morphologies of the electrolytic products can be engineered by manipulating the cations of the molten salts, carbonization procedures, and electrolysis variables, aiming to produce the high-performance LIB anodes from RHs (Figure 1).

2. Results

2.1. Synthesis of C-RHs

The first step is to convert RHs to C-RHs that contain the mixture of C and SiO₂. As reported, RHs contain amorphous hydrated silica (SiO₂ with 5–15 wt.% H₂O), lignin, cellulose, and hemicellulose.^[1f,18] After pyrolysis, the organic components are converted to hard C, and the RHs are converted to porous C-SiO₂ composites (Figure 1, Figure S2).

As shown in Figure 2 (a, e), C-RHs (Figure 2e) maintain the original geometries of RHs (Figure 2a), suggesting that the C-RHs inherit its original structure. The surface of RHs has arrays of protrusions along with some needle-like rods (Figure S3a) which can prevent the attack from insects. The surface of the protrusions is smooth and has a relatively higher

concentration of Si, which agrees well with the data reported by Choi et al.^[12b] In the meantime, C is distributed in the entire shell. Note that the surface of RHs also contains organic molecules to sustain the good mechanical strength and tenacity of the RHs. The structure of RHs is maintained (Figure S3, S4) after pyrolysis, and a skeleton-like structure (Figure 2e) could be due to the thermal decomposition of organic molecules. The inner side of the RHs also contains Si (Figure S3b), suggesting that Si distributes in the entire C-RHs. The RHs become black after pyrolysis (the inset of Figure 2e), indicating that the organic components are converted to carbon and the SiO₂ is encapsulated by the carbon even though the surface of RHs has a relatively high concentration of SiO₂.

The thermal decomposition of RHs was studied by the gravimetric analysis under both Ar and air atmospheres. From the TGA profile (Figure 3a), the weight loss of RHs in Ar involves three steps: (1) loss of water at ~100–165 °C; (2) initial thermal decomposition of cellulose, hemicellulose and lignin at ~165–300 °C; (3) further thermal decomposition of cellulose, hemicellulose and lignin to carbon at above 300 °C.^[19] After pyrolysis under Ar atmosphere, porous C-RHs were obtained (Figure S2a). The C-SiO₂ composite yield is 34 wt.% under Ar atmosphere (Figure 3a), and the SiO₂ yield is 16 wt.% in the air (Figure 3b) (supposing C is completely oxidized to CO₂ in the air and no other impurities exist). Accordingly, the C/SiO₂ mass ratio of the obtained C-SiO₂ composite is 18/16 which equals to a C/Si atom ratio of 5.6. The carbon content of the C-SiO₂ composite is too high because of the low energy density of C. As shown in Figure 3c, the SiO₂ and C in C-RHs are amorphous. The C and SiO₂ account for 55 wt.% of RHs (Figure 3d), meaning that 21% of C in the RHs is converted to gaseous products during the pyrolysis process. The carbon content can be further decreased by the calcination in the air.

2.2. Synthesis of the C-SiC Composite from C-RHs in Molten CaCl₂

The preparation of C-SiC composite was performed in molten CaCl₂, in which C-SiO₂ composite was electrochemically reduced to C-SiC at the cathode. Unlike the classic carbothermic reduction,^[20] the molten salt electrolysis approach employs electrons as the reducing agent and the operating temperature is below 1000 °C. More importantly, the components and morphologies of the electrolytic product can be rationalized by adjusting electrochemical variables. As shown in Figure 4a, the electrolytic product is the C-SiC composite under a constant cell voltage ranging from 2.4 to 2.8 V. Before electrolysis, C-RHs are irregular particles possessing a diameter of below 3 μm (Figure S2b). At 2.4 V, the electrolytic product contains SiC nanowires that are intricately distributed between amorphous C particles (Figure 4b). At 2.6 V, the electrolytic product contains honeycomb-like SiC wires, and the C particles disappear while C sheets appear (Figure 4c). As reported by Jin et al.,^[21] the C sheets could be attributed to the long-distance rearrangement of the atoms in amorphous C during the

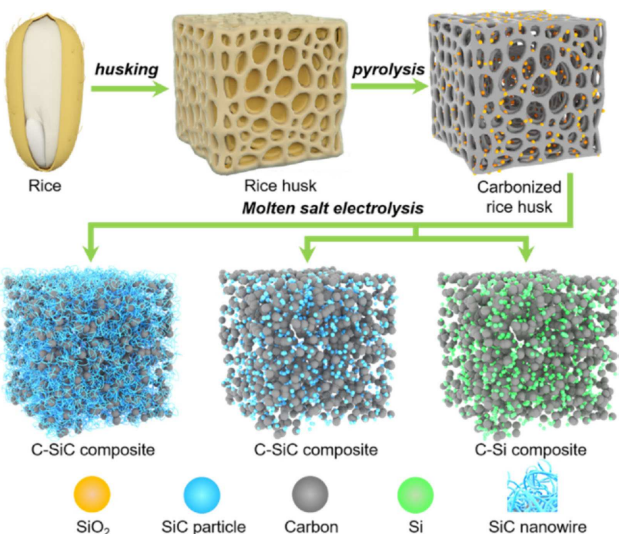


Figure 1. Schematic of the preparation of C–SiC and C–Si composites from RHs by the molten salt electrolysis approach.

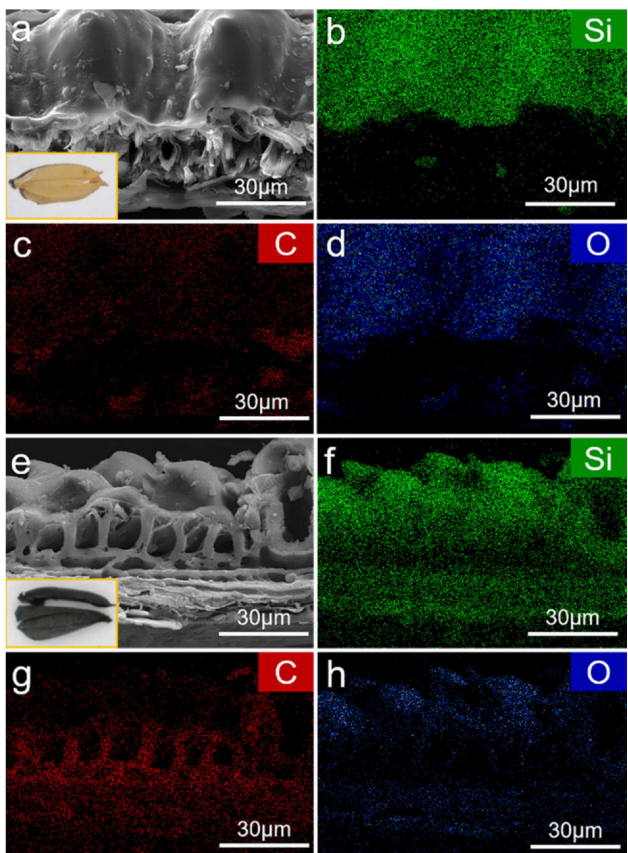


Figure 2. (a–d) Cross-sectional SEM image and EDS elemental mapping of RHs, (b) Si, (c) C, and (d) O. (e–h) Cross-sectional SEM image and EDS elemental mapping of C–RHs, (f) Si, (g) C, and (h) O.

electrolysis. Thus, the graphite sheets stem from the amorphous C. At 2.8 V, more C sheets along with the interconnected nanowires appear in the electrolytic product (Figure 4d). As shown in Figure 4e, SiC nanowires have a diameter of 8–10 nm

and the graphite flakes are overlapped with the SiC nanowires. Further, the measured lattice fringe spacing value is 0.25 nm, which corresponds to the SiC (111) lattice. The selected-area electron diffraction (SAED) (the inset picture of Figure 4f) also verifies that the crystalline structure of SiC contains the lattice plane spacing of (111), (220) and (311) lattice, which agrees well with the XRD patterns. Notably, Si is not observed in all three electrolytic products prepared at 2.4, 2.6 and 2.8 V. It has been reported that SiC was prepared by the electrochemical reduction of the mixture of SiO_2 and C,^[16a] and the electrolytic products were determined by the configuration of C and SiO_2 .^[16c,22] All electrolytic products are C–SiC composites, indicating that the SiO_2 and C are sufficiently contacted in the C–RHs. The current profiles of the electrolysis show typical characteristics of the electrochemical reduction of the solid cathode in molten salts, and the obtained products are black powders (Figure S5). As a result, the obtained SiC is thoroughly mixed with C, thereby increasing the electrical conductivity of the C–SiC composite, which is beneficial for improving the Li storage performance in LIBs.

The lithium storage performances of the electrolytic C–SiC composites were evaluated in the coin-type half cells containing a C–SiC composite working electrode and a Li foil counter electrode. As shown in Figure 5a, the cathodic peak at ~0.7 V is attributed to the formation of the solid-electrolyte interphase (SEI) layer in the first cathodic scan. The reduction peak at ~0.7 V disappears in the following cycles, indicating that the SEI layer is stable in the subsequent cycles. The discharge capacity of the C–SiC composite reaches 1235 mAh g^{-1} at a current density of 50 mA g^{-1} in the first cycle, and the initial Coulombic efficiency (ICE) is 65%. The relatively low ICE is mainly attributed to the formation of the SEI layer. The Coulombic efficiency gradually increases to 99% after 5 cycles. Unlike Si-based anodes having an obvious voltage plateau below 0.25 V (vs. Li^+/Li), the C–SiC anode has no obvious discharge voltage plateau (Figure 5b), which agrees with the CVs that do not have clear lithiation peaks prior to the deposition of Li (Figure 5a). The absence of the flat voltage plateau below 0.25 V suggests that the reduction process is due to the lithiation process of SiC.^[23] Further, the C–SiC anode has an excellent rate capability, delivering a specific capacity of 450 mAh g^{-1} at 1000 mA g^{-1} (Figure 5c). Different from the conventional anode materials, the specific capacity of C–SiC gradually increases with increasing the cycle number. The specific capacity increases to 1120 mAh g^{-1} at 500 mA g^{-1} after 600 cycles (Figure 5d). The incremental capacity of the C–SiC anode may be attributed to a slow and gradual crystal transformation in the cycling process.^[24] Thus, the active material retains a stable capacity of 1000 mAh g^{-1} at a current density of 1000 mA g^{-1} (Figure 5e). The specific capacity remains 790 mAh g^{-1} at a current density of 2000 mA g^{-1} after 500 cycles (Figure S6).

The SiC anode attracts limited attention because SiC has a poor electrical conductivity and super chemical stability. Dong et al.^[17a] synthesized the bowl-like 3 C–SiC encapsulated in hollow graphite carbon spheres that delivered a gravimetric capacity of 1000 mAh g^{-1} after 600 cycles. Moreover, the

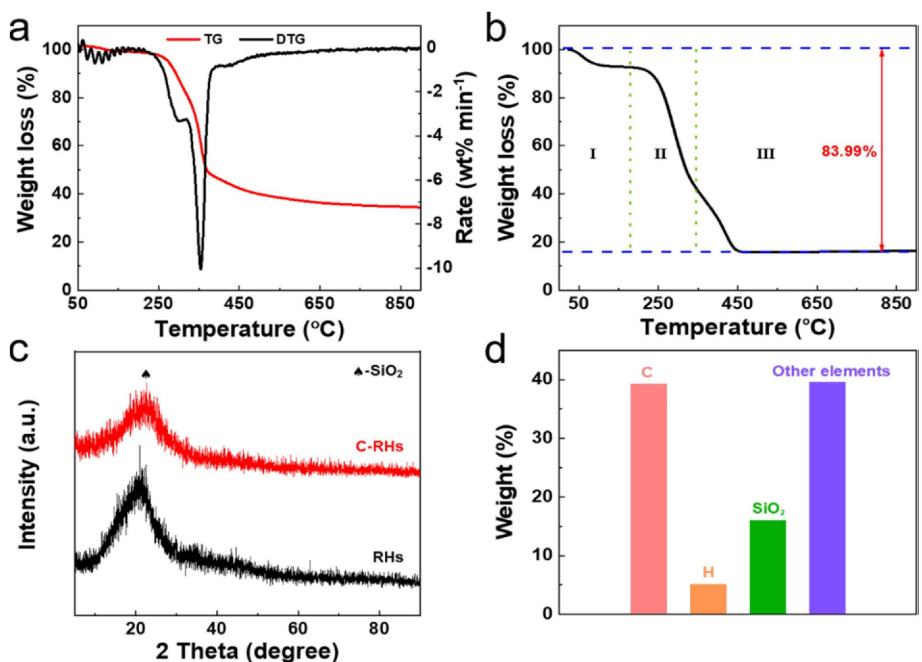


Figure 3. (a–b) TGA curves of the RHs under (a) Ar and (b) air atmospheres. (c) XRD patterns of the RHs and C–RHs. (d) Elemental analysis of the RHs.

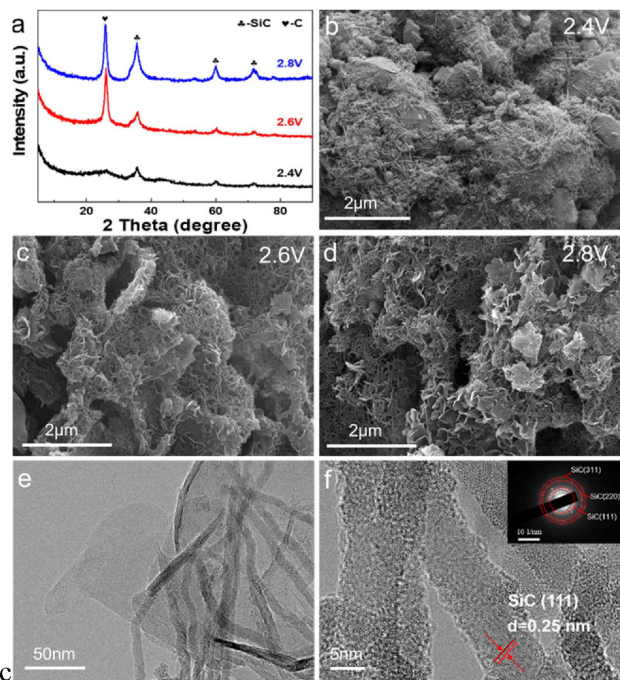


Figure 4. (a) XRD patterns and (b–d) SEM images of the electrolytic products obtained from the electrolysis of C–RHs (C:Si = 4.2:1, molar ratio) in molten CaCl₂ under (b) 2.4, (c) 2.6, and (d) 2.8 V. (e) TEM and (f) HRTEM images and the corresponding SAED pattern (the inset) of the electrolytic products obtained under 2.4 V in molten CaCl₂ at 850 °C.

capacity of the C–SiC composite anode increased with increasing the cycle number, which is in line with the cycling performance of the electrolytic C–SiC composite. The improved electrochemical performances of the SiC is attributed to the hollow structure of C which endows the electrical conductivity

and enhances the chemical activity of the SiC. In this regard, the high performance of the electrolytic C–SiC composite derived from RHs is due to the enhanced electrical conductivity and chemical activity of SiC nanowires (diameter < 10 nm).

2.3. Synthesis of the C–Si Composite from C–RHs in Molten NaCl–KCl–MgCl₂

The C–Si composite was prepared by the electrochemical reduction of C–RHs in molten NaCl–KCl–MgCl₂ (Figure 6a). The diffraction peaks of the electrolytic Si decrease with increasing the cell voltage because the lower cell voltage corresponds to a slower reduction rate that could increase the crystallinity of the electrolytic Si. In addition, a higher cell voltage enables the interplay of the Si and C. In previous studies, it is difficult to prepare the C–Si composite in molten CaCl₂ because of the formation of SiC.^[14d] Likewise, SiC also forms in both magnesio-thermic reduction^[25] and carbothermic reduction processes because the reaction of C and Si is spontaneous. Several approaches have been applied to prevent the formation of SiC by engineering the configurations of C/SiO₂, like creating buffer spaces between SiO₂ and C in the precursor.^[26] However, C and SiO₂ are naturally mixed in the growing process of the rice, thus it is difficult to make a buffer space between C and SiO₂. Hence, the MgCl₂-based molten salts play a crucial role in preventing the formation of SiC.

As shown in Figure 6b–f, the particle size of the electrolytic product is under 2 μm, which is different from that obtained in molten CaCl₂. Thus, the cations of molten salts significantly affect not only the components but also the morphologies of the electrolytic products. In addition, there is no graphite in the electrolytic products, indicating that the amorphous C cannot

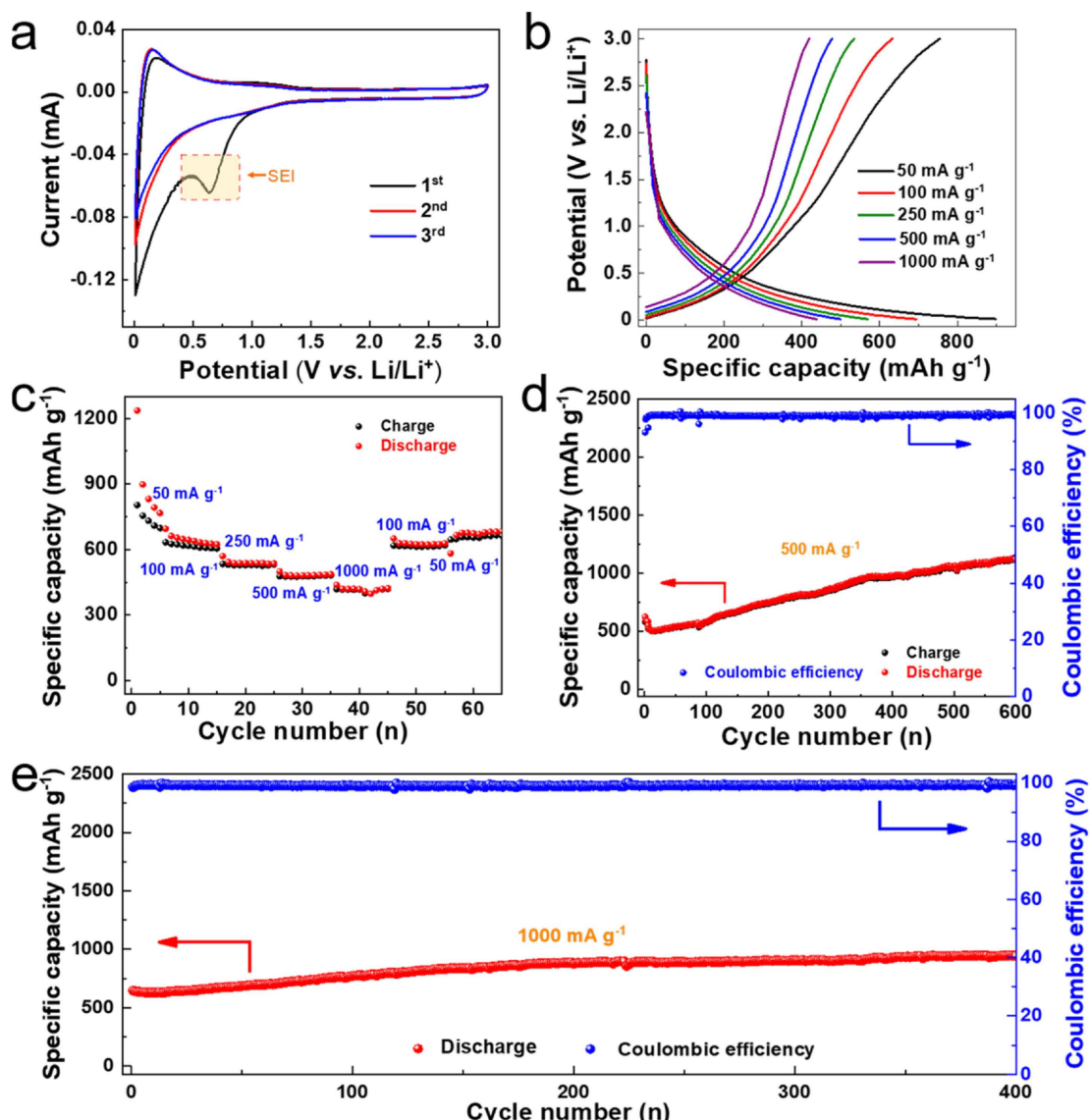


Figure 5. (a) Cyclic voltammograms (CVs) of the electrolytic product obtained from the electrolysis of C–RHs (C:Si = 4.2:1, molar ratio) in molten CaCl_2 and under 2.4 V, and the scan rate is 0.1 mV s^{-1} . (b) Charge-discharge profiles of the electrolytic product at current densities ranging from 50 to 1000 mA g^{-1} . (c) Rate capabilities of the electrolytic product at current densities ranging from 50 to 1000 mA g^{-1} . (d–e) Cycling performances and the corresponding Coulombic efficiencies of the electrode at 500 mA g^{-1} and 1000 mA g^{-1} , respectively.

be converted to graphite in molten $\text{NaCl}-\text{KCl}-\text{MgCl}_2$. To our surprise, SiC appears in the electrolytic products obtained at 2.6 V, and the morphologies of the SiC are different from the SiC nanowires obtained in molten CaCl_2 (Figure S6f). In this scenario, the electrolytic products are also related to the applied cell voltage of the electrolysis.

The electrochemical reduction behaviors of SiO_2 in molten $\text{NaCl}-\text{KCl}-\text{MgCl}_2$ were studied by cyclic voltammetry (Figure S7). Using an empty Mo cavity working electrode, a pair of redox peaks (c_1, a_1) at -1.5 V (vs. Ag) corresponds to the electrochemical deposition and stripping of Mg. A reduction peak (c_2) at -0.4 V is due to the reduction of SiO_2 , and a pair of redox peaks (c_3, a_3) is ascribed to the alloying and dealloying processes of Mg^{2+} with the electrolytic Si. In the second cycle, the reduction peak c_2 disappears because SiO_2 has been

completely reduced to Si. The results of CVs reveal that SiO_2 can be reduced to Si and the Mg^{2+} is then electrochemically alloyed with the Si to form Mg–Si alloys.

The C–RHs-derived electrolytic product is black (Figure S8) while the pure SiO_2 -derived electrolytic product is yellowish (Figure S9), suggesting that the carbon stays in the electrolytic products. Note that the rate of the electrolysis of the pure SiO_2 pellet in $\text{NaCl}-\text{KCl}-\text{MgCl}_2$ is slower than that of C– SiO_2 composite (C–RHs) because carbon increases the electrical conductivity of cathode thereby decreasing the IR drop. In addition, carbon also increases the electrical conductivity of the electrolytic C–Si composite since Si is a semiconductor at 660°C . Thus, carbon accelerates the rate of the electrochemical reduction of C–RHs in molten salt. As shown in Figure 6a, the C– SiO_2 pellet can be completely reduced to Si, suggesting that

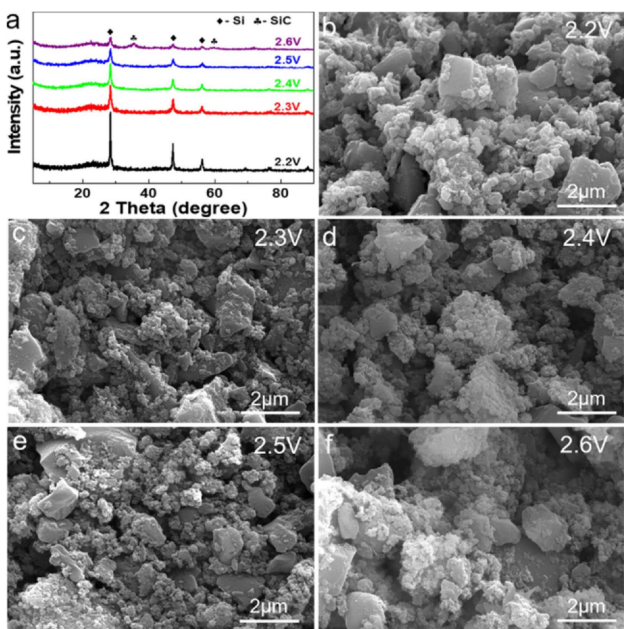


Figure 6. (a) XRD patterns of the electrolytic products obtained from the electrolysis of C–RHs (C:Si = 2.8:1, mole ratio) in molten NaCl–KCl–MgCl₂ at 660 °C. (b–f) SEM images of the electrolytic products obtained under (b) 2.2, (c) 2.3, (d) 2.4, (e) 2.5, and (f) 2.6 V.

the in situ generated MgO does not hinder the continuous reduction of SiO₂.

The lithium storage performances of the electrolytic C–Si composites were evaluated in the coin-type half-cells. As shown in Figure 7a, the reduction peak at 0.6 V (vs. Li⁺/Li) is due to the formation of the SEI layer and then a lithiation process takes place at 0.15 V. Upon the reverse scan, two delithiation processes take place at 0.35 and 0.53 V. It is found that the electrochemical behaviors of the C–Si composite are quite different from that of the C–SiC composite. For example, the voltage profile of the C–Si composite has an obvious plateau below 0.5 V, which is due to the alloying process of Li⁺ with Si (Figure 7b). The long flat discharge plateau (at 0.12 V vs. Li⁺/Li) corresponds to the lithiation of crystalline Si in the first cycle.^[27] However, the voltage profile of the electrolytic C–SiC composite has no voltage plateau below 0.5 V (Figure 5b). The C–Si composite exhibits an excellent rate performance with a capacity of 670 and 520 mAh g⁻¹ at 1000 mA g⁻¹ and 2000 mA g⁻¹, respectively (Figure 7c). The ICE of the C–Si composite is 57.3% owing to the formation of the SEI layer. As shown in Figure 7d, the specific capacity increases with increasing the cycle number in the initial 10 cycles, which may be attributed to the gradual activation of the electrode. After that, the C–Si composite anode delivers a specific capacity of 1069 mAh g⁻¹, and the capacity remains 926 mAh g⁻¹ after 100 cycles, corresponding to a capacity retention of 86.6%. Note that the relatively low specific capacity of the C–Si

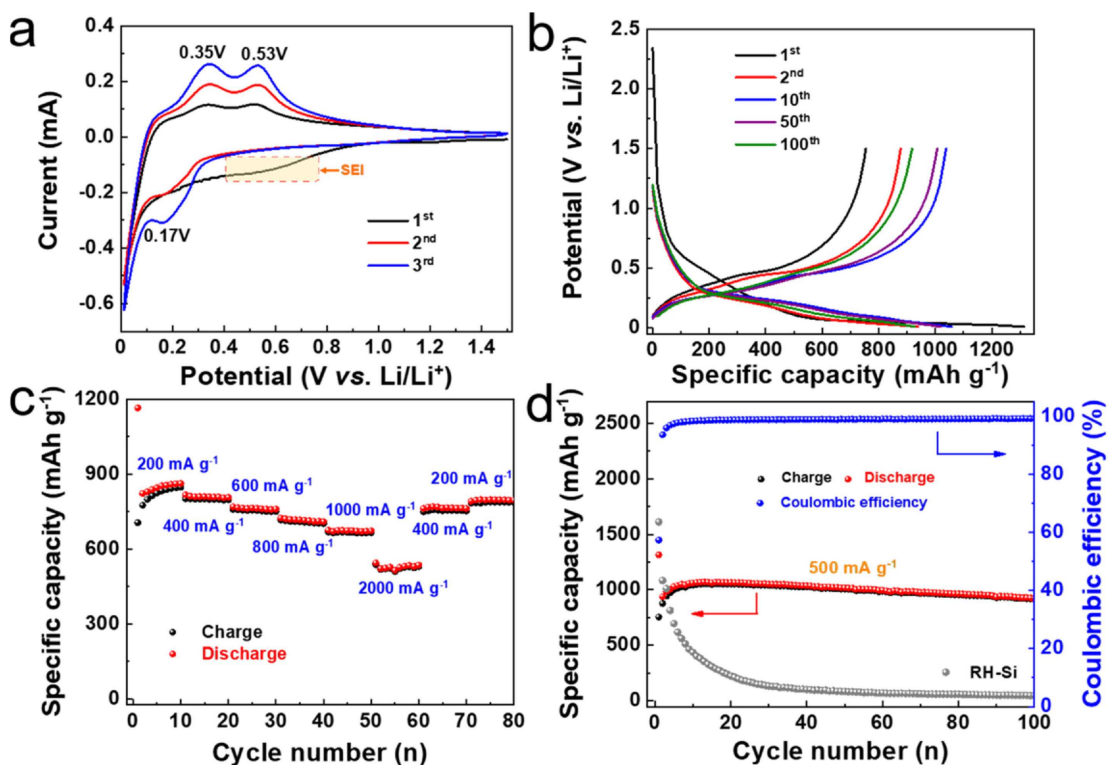


Figure 7. (a) CVs of the C–Si composite obtained from the electrolysis of C–RHs (C:Si = 2.8:1, molar ratio) in molten NaCl–KCl–MgCl₂ under 2.2 V (scan rate: 0.1 mV s⁻¹). (b) Charge-discharge profiles of the C–Si composite at a current density of 500 mA g⁻¹ for the 1st, 2nd, 10th, 50th, and 100th cycles. (c) Rate capabilities of the C–Si composite at current densities ranging from 200 to 2000 mA g⁻¹. (d) Cycling performances of the C–Si composite and RH-derived Si electrode at 500 mA g⁻¹.

composite is due to the relatively low Si content in the electrolytic C–Si composite. For example, the electrolytic C–Si composite contains 55 wt% of carbon, and the carbon only delivers a gravimetric capacity of less than 100 mAh g^{-1} (Figure S10). In addition, the particle size of the electrolytic C–Si composite is in micro-sized scale, so that the capacity is lower than that of the nanosized Si. The capacity of the electrolytic Si obtained from the pure SiO_2 drops from 1600 to 50 mAh g^{-1} after 50 cycles (Figure 7d), revealing that the electrolytic Si has poor cycling performances.

3. Discussions

3.1. Manipulation of Electrolytic Products (SiC or Si)

The compositions and morphologies of electrolytic products are different in molten CaCl_2 and $\text{NaCl}-\text{KCl}-\text{MgCl}_2$. Since the reaction of Si and C is spontaneous, SiC is termed as the thermodynamically favored product.^[26b] Thus, the component of electrolytic products can be solely adjusted by engineering the kinetic process. Note that the contact of C and SiO_2 is crucial to promoting the generation of SiC .^[16c, 26b] However, it is difficult to engineer the configuration of C and SiO_2 in C–RHs because they grow together. In molten CaCl_2 , only SiC is obtained from the electrochemical reduction of the C–RHs under various potentials, which has been confirmed by many research groups.^[14d, 16, 28] In molten CaCl_2 , SiO_2 is reduced to Si at the cathode that releases O^{2-} into the molten CaCl_2 , and then the O^{2-} moves towards the anode and is discharged as CO_2/CO at the carbon anode. In molten MgCl_2 -based melts, the released O^{2-} will form insoluble MgO and, to keep the charge balance, the Cl^- ions will be oxidized to Cl_2 at the carbon anode. Inspired by both molten salt electrolysis and magnesiothermic reduction, Mg^{2+} could be an important mediator to tune the electrolytic products in molten salt.^[29] First, MgO is more stable than SiO_2 so that SiO_2 can be reduced to Si prior to the deposition of Mg in MgCl_2 -based molten salts (Figure 8). Moreover, the reduction of SiO_2 will generate insoluble MgO which may act as a buffer to prevent the generation of SiC ,^[30] which is different from the CaCl_2 that has a high solubility of CaO .^[31]

Thermodynamically, SiC is more stable than the C–Si composite because of the negative Gibbs free energy of formation of the reaction of Si and C. Thus, the electrolytic C–Si composite is the kinetically favored product. In the molten $\text{NaCl}-\text{KCl}-\text{MgCl}_2$, the in situ generated MgO is not soluble in the molten salt and may act as a buffer to prevent adequate contact between Si and C (Figure S11). However, the magnesiothermic reduction of C– SiO_2 generates SiC with the presence of in situ formed MgO .^[25] Thus, the generated MgO cannot fully prevent the growth of SiC . On the other hand, the electrolytic product can be tuned by altering the electrolysis cell voltage. For example, the electrolytic product is SiC when the cell voltage is higher than 2.5 V. According to the standard potential profile (Figure 8b), Mg–Si and Mg will be generated at the cathode with increasing the cell voltage. Consequently,

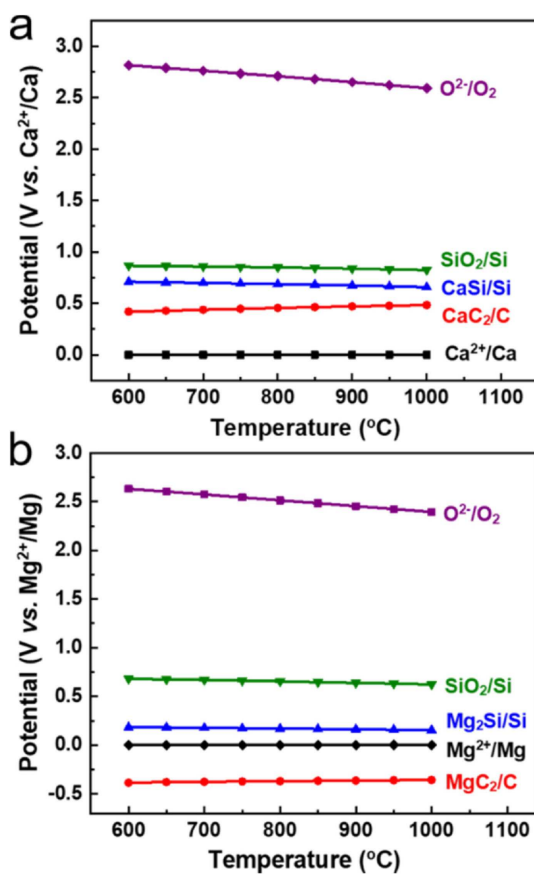


Figure 8. Profiles of the standard potentials of several reactions as a function of temperature in (a) molten CaCl_2 and (b) MgCl_2 .

the formation of Mg or Mg–Si alloys may promote the generation of SiC , which is identical to the magnesiothermic reduction that the reduction takes place in the presence of Mg and Mg–Si. Thermodynamically, Mg and Mg–Si alloys will be produced when the cell voltage is higher than 2.5 V, and the produced Mg and Mg–Si alloys may enhance the kinetic of the carbidization. Note that the intermediate Mg and Mg–Si alloys can react with SiO_2 to generate Si and simultaneously the Si reacts with C to generate SiC . Hence, the electrolytic product is SiC when the cell voltage is higher than 2.5 V, and increasing the cell voltage is able to overcome the kinetic barrier of the formation of SiC . Mg–Si alloys were obtained when the cathode was pure Si.^[32] Therefore, the intermediate Mg and Mg–Si alloys may form at 2.6 V and the intermediates could enhance the reaction kinetics of Si and C in molten $\text{NaCl}-\text{KCl}-\text{MgCl}_2$.

Unlike in molten $\text{NaCl}-\text{KCl}-\text{MgCl}_2$, the formation of CaC_2 takes place at a potential more positive than that of the deposition of Ca in molten CaCl_2 (Figure 8a). The formation of CaC_2 is helpful to induce the formation of SiC because the reaction of CaC_2 with SiO_2 can generate SiC and the reaction is spontaneous. As reported,^[16c, 26b] the reaction of Si and C is governed by the contact surface area of Si and C. Since the CaO has a high solubility in molten CaCl_2 , the generated CaO will dissolve in the molten salt, allowing the sufficient contact of Si and C. Thus, SiC is the only electrolytic product by the

electrolysis of C–RHs in molten CaCl_2 . However, MgC_2 forms at a potential more negative than Mg in molten $\text{NaCl}-\text{KCl}-\text{MgCl}_2$. So that it is difficult to generate MgC_2 in molten $\text{NaCl}-\text{KCl}-\text{MgCl}_2$. This could be another reason that the C–Si can be prepared in $\text{NaCl}-\text{KCl}-\text{MgCl}_2$ but it is difficult to prepare Si in molten CaCl_2 by the electrolysis of C–RHs.

3.2. Lithium Storage Performances of SiC of Different Morphologies

The Li storage performances of the SiC prepared under different conditions were evaluated. The C–SiC composite obtained in molten CaCl_2 (denoted as C–SiC-2.4 V– CaCl_2) delivers a capacity of 1000 mAh g^{-1} at 500 mA g^{-1} after 600 cycles (Figure 5d). The electrolytic samples C–SiC-2.6 V– CaCl_2 (Figure S12) and C–SiC-2.8 V– CaCl_2 (Figure S13) deliver a capacity of 750 and 850 mAh g^{-1} at 100 mA g^{-1} after 400 and 375 cycles, respectively. Thus, the amorphous C is beneficial for improving the capacity and the rate capability of the C–SiC composite, which is ascribed to the configuration of SiC with the amorphous C. According to the thermodynamic analysis (Figure 8a), CaC_2 forms at a more negative potential than that of Si. The generation of CaC_2 will break the big carbon particles thereby forming SiC nanowires and C networks. The growth mechanism of SiC nanowires is not clear and needs further research.

Moreover, the obtained SiC from the carbothermic reduction (denoted as CT–SiC) delivers a much lower capacity than that of the electrolytic products in molten CaCl_2 . The CT–SiC-1600 (Figure S14) and CT–SiC-1500 composites (Figure S15) deliver a capacity of 400 and 380 mAh g^{-1} at 50 mA g^{-1} after 500 cycles. As shown in Figure S16a, C–RHs were completely converted to SiC at 1500°C . The rod-like SiC has a diameter of over 100 nm for all CT–SiC samples (Figure S16b–d). Compared with the electrolytic samples, the size of CT–SiC is much larger than that of the electrolytic products, thus leading to the poor Li storage performances.

3.3. Altering the Si/C Ratio of C–Si Composites

The gravimetrical capacity of the C–Si composite anode is associated with the C content because the capacity of C is much lower than that of Si. The C/Si atom ratio of C–RHs obtained in Ar atmosphere is 5.6, which is too high to prepare C–SiC and C–Si composites. When the C/Si atom ratio decreases to 4.2 (Figure S17), the electrolytic C–Si composite delivers a capacity of 275 mAh g^{-1} at a current density of 200 mA g^{-1} after 160 cycles (Figure S18). Note that the capacity of the RHs-derived amorphous C anode is $\sim 100 \text{ mAh g}^{-1}$ at 200 mA g^{-1} (Figure S10). When the C/Si atom ratio decreases to 2.8, the electrolytic C–Si composite delivers a capacity of 926 mAh g^{-1} at a current density of 500 mA g^{-1} after 100 cycles (Figure 7d). Hence, the calcination of RHs in the air can be used to reduce the C content so as to increase the gravimetrical capacities of the electrolytic products. More efforts are needed

to optimize the C content and engineer the structure of C–SiO₂ composite, thereby improving the Li storage performances of the electrolytic C–SiC and C–Si composites.

4. Conclusions

The extraction of C–SiC and C–Si composites from RHs by the molten salt electrolysis approach has been proven to be a straightforward and efficient way to prepare high-performance LIB anodes. The cations of molten salts play a key role in determining the electrolytic products, i.e., the C–SiC nanowire composite was obtained in molten CaCl_2 , and the C–Si composite was obtained in molten $\text{NaCl}-\text{KCl}-\text{MgCl}_2$. The obtained C–SiC nanowire composite delivered a gravimetric capacity of 1000 mAh g^{-1} at 1000 mA g^{-1} after 400 cycles, and the C–Si composite delivered a gravimetric capacity of 926 mAh g^{-1} at 500 mA g^{-1} and with a capacity retention of 86.6% after 100 cycles. Compared with the C–SiC composites prepared in different conditions, the superior battery performance of the C–SiC nanowire composite owes to the small diameter of SiC ($< 10 \text{ nm}$) and the amorphous C. More efforts are needed to further valorize the carbon in RHs and engineer the natural porous structure. Overall, the molten salt electrolysis approach harvests both C and Si from the RHs, providing sustainable and carbon-neutral resources to produce energy storage materials.

Acknowledgements

We greatly thank the financial support from National Thousand Youth Talent Program of China, Fundamental Research Funds for the Central Universities (N172505002), the National Key R&D Program of China (2017YFB0305401), NSFC (51704060), and the 111 Project (B16009).

Conflict of Interest

The authors declare no conflict of interest.

Keywords: rice husk • molten salt electrolysis • lithium-ion batteries • silicon • silicon carbide

- [1] a) Y. Cui, C. M. Lieber, *Science* **2001**, *291*, 851–853; b) D. D. Tune, B. S. Flavel, R. Krupke, J. G. Shapter, *Adv. Energy Mater.* **2012**, *2*, 1043–1055; c) R. Teki, M. K. Datta, R. Krishnan, T. C. Parker, T. M. Lu, P. N. Kumta, N. Koratkar, *Small*, **2009**, *5*, 2236–2242; d) S. J. Kang, C. Kocabas, T. Ozel, M. Shim, N. Pimparkar, M. A. Alam, S. V. Rotkin, J. A. Rogers, *Nat. Nanotechnol.* **2007**, *2*, 230–236; e) L. M. Dai, D. W. Chang, J. B. Baek, W. Lu, *Small*, **2012**, *8*, 1130–1166; f) H. Chen, W. Wang, J. C. Martin, A. J. Oliphant, P. A. Doerr, J. F. Xu, K. M. Deborn, C. X. Chen, L. Y. Sun, *ACS Sustainable Chem. Eng.* **2013**, *1*, 254–259; g) B. Ma, B. Lu, J. Luo, X. Deng, Z. Wu, X. Wang, *Electrochim. Acta* **2018**, *288*, 61–70.
- [2] a) N. Nitta, F. Wu, J. T. Lee, G. Yushin, *Mater. Today* **2015**, *18*, 252–264; b) V. Etacheri, R. Marom, R. Elazari, G. Salitra, D. Aurbach, *Energy Environ. Sci.* **2011**, *4*, 3243–3262; c) B. Lu, B. Ma, X. Deng, B. Wu, Z. Wu, J. Luo, X. Wang, G. Chen, *Chem. Eng. J.* **2018**, *351*, 269–279.

- [3] a) L. Y. Yang, H. Z. Li, J. Liu, Z. Q. Sun, S. S. Tang, M. Lei, *Sci. Rep.* **2015**, *5*, 10908; b) R. Zhang, Y. Du, D. Li, D. Shen, J. Yang, Z. Guo, H. K. Liu, A. A. Elzatahry, D. Zhao, *Adv. Mater.* **2014**, *26*, 6749–6755; c) B. Ma, J. Luo, X. Deng, Z. Wu, Z. Luo, X. Wang, Y. Wang, *ACS Appl. Nano Mater.* **2018**, *1*, 6989–6999; d) J. Luo, B. Ma, J. Peng, Z. Wu, Z. Luo, X. Wang, *ACS Sustainable Chem. Eng.* **2019**, *7*, 10415–10424.
- [4] a) S. Chu, Y. Cui, N. Liu, *Nat. Mater.* **2017**, *16*, 16–22; b) I. H. Son, J. H. Park, S. Kwon, S. Park, M. H. Ruemmeli, A. Bachmatiuk, H. J. Song, J. Ku, J. W. Choi, J. M. Choi, S. G. Doo, H. Chang, *Nat. Commun.* **2015**, *6*, 7393.
- [5] a) D. T. Ngo, H. T. T. Le, X.-M. Pham, J. W. Jung, N. H. Vu, J. G. Fisher, W. B. Im, I. D. Kim, C. J. Park, *J. Mater. Chem. A* **2018**, *6*, 2834–2846; b) K. Yasuda, T. H. Okabe, *JOM* **2010**, *62*, 94–101; c) A. Vignes, *Extr Metall* **1**, Vol. 1, John Wiley & Sons, Inc., London, 2011.
- [6] a) Z. L. Xu, X. Liu, Y. Luo, L. Zhou, J. K. Kim, *Pro. Mater. Sci.* **2017**, *90*, 1–44; b) M. L. Terranova, S. Orlanducci, E. Tamburri, V. Guglielmotti, M. Rossi, *J. Power Sources* **2014**, *246*, 167–177.
- [7] a) X. Su, Q. Wu, J. Li, X. Xiao, A. Lott, W. Lu, B. W. Sheldon, J. Wu, *Adv. Energy Mater.* **2014**, *4*, 1300882; b) H. Okamoto, Y. Sugiyama, H. Nakano, *Chem. Eur. J.* **2011**, *17*, 9864–9887.
- [8] J. Entwistle, A. Rennie, S. Patwardhan, *J. Mater. Chem. A* **2018**, *6*, 18344–18356.
- [9] a) Y. C. Zhang, Y. You, S. Xin, Y. X. Yin, J. Zhang, P. Wang, X. S. Zheng, F. F. Cao, Y. G. Guo, *Nano Energy* **2016**, *25*, 120–127; b) B. Li, Z. Xiao, M. Chen, Z. Huang, X. Tie, J. Zai, X. Qian, *J. Mater. Chem. A* **2017**, *5*, 24502–24507; c) Y. Shen, *Renewable Sustainable Energy Rev.* **2017**, *80*, 453–466; d) Y. Shen, *J. Agric. Food Chem.* **2017**, *65*, 995–1004; e) W. Long, B. Fang, A. Ignaszak, Z. Wu, Y. J. Wang, D. Wilkinson, *Chem. Soc. Rev.* **2017**, *46*, 7176–7190.
- [10] a) J. F. Ma, K. Tamai, N. Yamaji, N. Mitani, S. Konishi, M. Katsuhara, M. Ishiguro, Y. Murata, M. Yano, *Nature* **2006**, *440*, 688–691; b) J. F. Ma, N. Yamaji, *Trends Plant Sci.* **2006**, *11*, 392–397.
- [11] M. Estevez, S. Vargas, V. M. Castaño, R. Rodriguez, *J. Non-Cryst. Solids* **2009**, *355*, 844–850.
- [12] a) L. Y. Sun, K. C. Gong, *Ind. Eng. Chem. Res.* **2001**, *40*, 5861–5877; b) D. S. Jung, M. H. Ryou, Y. J. Sung, S. B. Park, J. W. Choi, *Proc. Natl. Acad. Sci. USA* **2013**, *110*, 12229–12234.
- [13] a) Y. Shen, P. Zhao, Q. Shao, *Microporous Mesoporous Mater.* **2014**, *188*, 46–76; b) S. Artkla, W. Kim, W. Choi, J. Wittayakun, *Appl. Catal. B* **2009**, *91*, 157–164; c) N. Grisdanurak, S. Chiarakorn, J. Wittayakun, *Korean J. Chem. Eng.* **2003**, *20*, 950–955; d) X. Wang, H. C. Schroder, M. Wiens, H. Ushijima, W. E. Muller, *Curr. Opin. Biotechnol.* **2012**, *23*, 570–578; e) J. Athinarayanan, V. S. Periasamy, M. Alhazmi, K. A. Alatiah, A. A. Alshatwi, *Ceram. Int.* **2015**, *41*, 275–281; f) J. Suwanprateeb, K. Hatthanapant, *J. Appl. Polym. Sci.* **2002**, *86*, 3013–3020; g) Z. Wang, A. T. Smith, W. Wang, L. Y. Sun, *Angew. Chem. Int. Ed. Engl.* **2018**, *57*, 13722–13734.
- [14] a) G. Z. Chen, D. J. Fray, T. W. Farthing, *Nature* **2000**, *407*, 361–364; b) A. M. Abdelkader, K. T. Kilby, A. Cox, D. J. Fray, *Chem. Rev.* **2013**, *113*, 2863–2886; c) W. Xiao, D. Wang, *Chem. Soc. Rev.* **2014**, *43*, 3215–3228; d) J. Fan, Y. Yang, D. Tang, W. Xiao, X. Mao, D. Wang, *J. Electrochem. Soc.* **2017**, *164*, E144–E150; e) A. Allanore, L. Yin, D. R. Sadoway, *Nature* **2013**, *497*, 353–356; f) H. Y. Yin, B. Chung, D. R. Sadoway, *Nat. Commun.* **2016**, *7*, 5; g) R. O. Suzuki, M. Aizawa, K. Ono, *J. Alloys Compd.* **1999**, *288*, 173–182; h) X. Guan, U. B. Pal, *Prog. Nat. Sci.: Mater. Int.* **2015**, *25*, 591–594; i) S. Sokhanvaran, S.-K. Lee, G. Lambotte, A. Allanore, *J. Electrochem. Soc.* **2016**, *163*, D115–D120.
- [15] a) T. Nohira, K. Yasuda, Y. Ito, *Nat. Mater.* **2003**, *2*, 397–401; b) X. Jin, P. Gao, D. Wang, X. Hu, G. Z. Chen, *Angew. Chem. Int. Ed.* **2004**, *43*, 733–736; *Angew. Chem.* **2004**, *116*, 751–754; c) Y. Dong, T. Slade, M. J. Stolt, L. Li, S. N. Girard, L. Mai, S. Jin, *Angew. Chem. Int. Ed. Engl.* **2017**, *56*, 14453–14457; d) X. Yang, L. Ji, X. Zhou, T. Lim, J. Zhao, E. T. Yu, A. J. Bard, *Angew. Chem. Int. Ed. Engl.* **2017**, *56*, 15078–15082.
- [16] a) X. Zou, L. Ji, X. Lu, Z. Zhou, *Sci. Rep.* **2017**, *7*, 9978; b) D. S. M. Vishnu, J. Sure, H. K. Kim, J. Y. Kim, C. R. V. Kumar, C. Schwandt, *J. Electrochem. Soc.* **2018**, *165*, D731–D742; c) H. J. Zhao, H. W. Xie, X. B. Zhou, J. K. Qu, Z. Q. Zhao, Q. S. Song, Z. Q. Ning, P. F. Xing, H. Y. Yin, *J. Electrochem. Soc.* **2019**, *166*, E137–E143.
- [17] a) H. W. Li, H. J. Yu, X. F. Zhang, G. N. Guo, J. H. Hu, A. G. Dong, D. Yang, *Chem. Mater.* **2016**, *28*, 1179–1186; b) T. K. Bijoy, J. Karthikeyan, P. Murugan, *J. Phys. Chem. C* **2017**, *121*, 15106–15113; c) X. Sun, C. Shao, F. Zhang, Y. Li, Q. H. Wu, Y. Yang, *Front. Chem.* **2018**, *6*, 166; d) H. Zhang, H. Xu, *Solid State Ionics* **2014**, *263*, 23–26.
- [18] E. Hermann, K. D. Demadis, O. S. Pokrovsky, P. G. Koutsoukos, *Chem. Rev.* **2010**, *110*, 4656–4689.
- [19] D. Kalderis, S. Bethanis, P. Paraskeva, E. Diamadopoulos, *Bioresour. Technol.* **2008**, *99*, 6809–6816.
- [20] a) R. B. Wu, K. Zhou, C. Y. Yue, J. Wei, Y. Pan, *Prog. Mater. Sci.* **2015**, *72*, 1–60; b) C. T. Wei, *J. Am. Ceram. Soc.* **1983**, *66*, C111.
- [21] X. B. Jin, R. He, S. Dai, *Chem. Eur. J.* **2017**, *23*, 11455–11459.
- [22] W. Weng, C. Zeng, W. Xiao, *ACS Appl. Mater. Interfaces* **2019**, *11*, 9156–9163.
- [23] T. S. D. Kumari, D. Jeyakumara, T. P. Kumar, *RSC Adv.* **2013**, *3*, 15028–15034.
- [24] T. Sri Devi Kumari, D. Jeyakumar, T. Prem Kumar, *RSC Adv.* **2013**, *3*, 15028–15034.
- [25] J. Su, B. Gao, Z. Chen, J. Fu, W. An, X. Peng, X. Zhang, L. Wang, K. Huo, P. K. Chu, *ACS Sustainable Chem. Eng.* **2016**, *4*, 6600–6607.
- [26] a) S. Chen, L. Shen, P. A. van Aken, J. Maier, Y. Yu, *Adv. Mater.* **2017**, *29*, 1605650; b) J. Ahn, H. S. Kim, J. Pyo, J. K. Lee, W. C. Yoo, *Chem. Mater.* **2016**, *28*, 1526–1536.
- [27] Y. Xu, Y. Zhu, F. Han, C. Luo, C. Wang, *Adv. Energy Mater.* **2015**, *5*, 1400753.
- [28] C. Zhao, J. Yang, S. Lu, *Chinese J. Inorg. Chem.* **2013**, *29*, 2543–2548.
- [29] H. W. Xie, H. J. Zhao, J. K. Qu, Q. S. Song, Z. Q. Ning, H. Y. Yin, *J. Solid State Electrochem.* **2019**, *23*, 903–909.
- [30] Y. Yuan, W. Li, H. Chen, Z. Wang, X. Jin, G. Z. Chen, *Faraday Discuss.* **2016**, *190*, 85–96.
- [31] S. L. Wang, F. S. Zhang, X. Liu, L. J. Zhang, *Thermochim. Acta* **2008**, *470*, 105–107.
- [32] Y. T. Yuan, W. Xiao, Z. Y. Wang, D. J. Fray, X. B. Jin, *Angew. Chem. Int. Ed. Engl.* **2018**, *57*, 15743–15748.

Manuscript received: July 4, 2019

Revised manuscript received: August 22, 2019

Accepted manuscript online: September 5, 2019

Version of record online: September 12, 2019